Magnetic Resonance in Medicine 46:379–385 (2001)

Radio Frequency Magnetic Field Mapping of a 3 Tesla Birdcage Coil: Experimental and Theoretical Dependence on Sample Properties

Marcello Alecci,[1*] Christopher M. Collins,[2] Michael B. Smith,[2] and Peter Jezzard[1]

The RF B_1 distribution was studied, theoretically and experimentally, in phantoms and in the head of volunteers using a 3 T MRI system equipped with a birdcage coil. Agreement between numerical simulation and experiment demonstrates that B_1 distortion at high field can be explained with 3D full-Maxwell calculations. It was found that the B_1 distribution in the transverse plane is strongly dependent on the dielectric properties of the sample. We show that this is a consequence of RF penetration effects combined with RF standing wave effects. In contrast, along the birdcage coil z-axis the B_1 distribution is determined mainly by the coil geometry. In the transverse plane, the region of B_1 uniformity (within 10% of the maximum) was 15 cm with oil, 6 cm with distilled water, 11 cm with saline, and 10 cm in the head. Along z the B_1 uniformity was 9 cm with phantoms and 7 cm in the head. Magn Reson Med 46:379–385, 2001.

Key words: high field MRI; RF mapping; birdcage coil; human brain

The recent development of high-efficiency head gradient coils and ultrafast MRI pulse sequences has allowed an impressive number of functional MRI studies in human brain research to be realized. The need for higher sensitivity has pushed current MRI research towards the development of high field (>1.5 T) MRI systems (1). However, magnetic field inhomogeneity and susceptibility artifacts increase with field strength, requiring the development of methods to evaluate and, possibly, eliminate their effects (2). Even if the problems of B_0 magnetic field susceptibility were to be solved, the effect of RF magnetic field (B_1) inhomogeneity has long been recognized as a potential source of image artifacts in high field systems (3,4). In fact, for frequencies higher than 64 MHz the RF eddy currents induced in the human body cannot be neglected. Moreover, because the effective wavelength of the RF field is comparable to or smaller than the dimension of the human body, there is a significant variation of the B_1 phase along the sample (3). This gives B_1 standing wave effects and consequently the RF field homogeneity can be strongly degraded. As a further consideration, at high field the distribution of the power deposition caused by the RF irradiating field must be carefully considered for safety reasons and strict limits on the specific absorption rate (SAR) have been established (5,6).

Because of the complex anatomical structure of the human head, it is impossible to analytically evaluate the RF B_1 spatial distribution. In the past few years, for RF coils operating between 64 MHz and 341 MHz, numerical electromagnetic (EM) computational techniques have been developed to evaluate the B_1 and the SAR in phantoms and in the human head (7–13). Although very powerful, these numerical techniques use a simplified model of the human head (typically, 2 mm voxel, up to 20 tissues, measured or interpolated/extrapolated dielectric properties of tissues). The effects of head size, position, and motion within the RF coil have not been considered. Additionally, they make many assumptions about the RF coil modeling (intrinsic RF B_1 distribution, coil losses, effective coil length, perfect circular polarization, etc.). Birdcage coils (14) provide a very homogeneous RF field at low static magnetic field (≤1.5 T) and, as such, are widely used for clinical MRI studies. At these low fields the intrinsic B_1 inhomogeneities along the coil z axis are not considered a limiting factor. However, for human brain applications the anatomical constraints require a short birdcage coil (shield length less than 35 cm). Conversely, at high field the RF wavelength is comparable to or shorter than the length of the coil elements (typically less than 25 cm) and a standing wave pattern of the RF currents along the coil axis is predicted (8,15). This effect should produce a significant B_1 inhomogeneity along the coil axis (sagittal/coronal plane) and theoretical modeling predicts a dependence on the operating frequency, the coil size, the shield dimensions, the sample size, and the dielectric characteristics of the sample (15).

For these reasons, in high field MRI systems it is desirable to accurately map B_1 with suitable phantoms and, ultimately, in vivo. Several workbench (16,17) and MRI-based (18–21) techniques have been previously reported for B_1 mapping. Usually, the B_1 amplitude in a single voxel is derived from the ratio of gradient-echo or spin-echo MRI images obtained at two different flip angles. Recently, a B_1 mapping technique that uses a collection of four stimulated-echo (STE) MRI images obtained at different flip angles has been reported using a phantom (22) and in the human head (23) at 1.5 T. A multipower B_1 mapping technique that uses a large collection of spin-echo (SE) MRI images obtained over a wide range of transmitter powers has been reported at 1.5 T (24).

We report the theoretical and experimental RF B_1 distribution in phantoms and in the head of healthy volunteers

[1]Centre for Functional Magnetic Resonance Imaging of the Brain, Department of Clinical Neurology, John Radcliffe Hospital, University of Oxford, Headington, Oxford, UK.

[2]Center for NMR Research, Department of Radiology, H066, Penn State College of Medicine, Hershey, PA.

Grant sponsors: EU BIOMED; UK MRC.

This work is dedicated in memory of Jason A. Brookes, Ph.D.

*Correspondence to: Dr. M. Alecci, FMRIB Centre, John Radcliffe Hospital, University of Oxford, Headington, Oxford OX3 9DU, UK. E-mail: alecci@fmrib.ox.ac.uk

Received 22 June 2000; revised 12 February 2001; accepted 20 February 2001.

using a 3 T MRI research system equipped with a birdcage coil.

MATERIALS AND METHODS

3 T Scanner

The 3 T human MRI research system is composed of a 1 m bore superconducting magnet with 22 tons of passive shielding (Oxford Magnet Technology, Oxford, UK). A head gradient coil (Magnex, Abingdon, UK, model SGRAD MKIII) is housed in the bore. The inside diameter of the Magnex coil is 38 cm and it provides a maximum gradient strength of 34 mT/m in a minimum of 200 μs. The magnet is driven by a Varian console (Varian, Palo Alto, CA, Unity Inova) connected to gradient amplifiers (Siemens Medical Systems, South Iselin, NJ; GPS, 600 V-250 A) and a 4 kW RF amplifier (American Microwave Technology, Anaheim, CA, Model 4T40). The system is equipped with a 16-element quadrature birdcage coil (dia. 27.8 cm, length 21 cm) used for pulse transmission and signal reception (25). An RF copper shield (dia. 37.6 cm, length 27 cm, thickness 5 μm) was employed to reduce radiating losses and parasitic coupling with the head gradient coil.

Workbench B_1 Mapping

A network analyzer (Hewlet-Packard, Bracknell, UK, HP8712C) was used to measure the resonant frequency (f_0 = 127.3 MHz), the reflection coefficient (S_{11}), and the quality factor (Q) of the birdcage coil. A small pick-up probe (8 turns, 12 mm dia., 9 mm length) connected to a high-frequency oscilloscope (Hewlet-Packard, HP54610B) was used to measure the RF field in the axial direction, $B_1(z)$, and in the transverse directions, $B_1(x)$ or $B_1(y)$, of the empty coil. The HP8712C was connected in turn to one channel of the RF coil (linear polarization along x or y) and acted as a CW transmitter. A mechanical sliding device allowed the pick-up probe to be shifted within the birdcage coil with an accuracy of ±1 mm. Using the pick-up probe the measured efficiency ($\Lambda = B_1/\sqrt{\text{Pcoil}}$) at the center of the RF coil when empty was 0.06 $\mu T/\sqrt{W}$ (rotating frame component per channel).

MRI B_1 Mapping

To illustrate the effect of RF B_1 inhomogeneity with the head coil at 3 T, transaxial and coronal MRI images are shown in Fig. 1a,b, respectively. A spin-echo MRI pulse sequence was used with TE = 15 ms, TR = 0.6 sec, and slice thickness = 5 mm. It is evident that the MRI signal amplitude is affected by a significant RF inhomogeneity along the transverse and the axial dimensions.

These B_1 inhomogeneities were studied further using a multipower MRI-based B_1 mapping technique (24). This is based on a spin-echo pulse sequence and requires the collection of a set of images over a broad range of flip angles, i.e., transmitter (TX) powers. Using the birdcage coil in transmit/receive mode and selecting the appropriate TE and TR (to minimize T_1 and T_2 relaxation effects), the signal intensity at a given position r is related to the B_1 amplitude at the same position by (24):

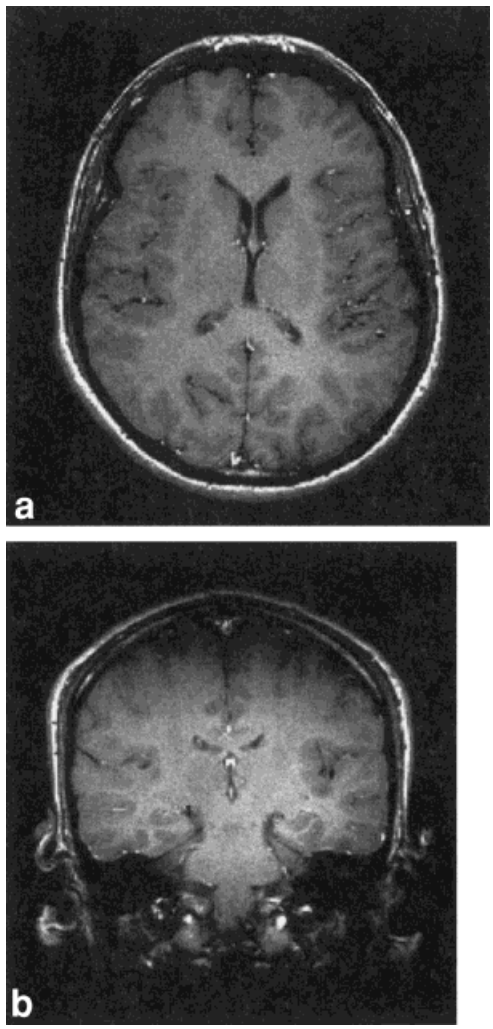

FIG. 1. Transaxial (**a**) and coronal (**b**) spin-echo MRI image obtained at 3 T with TE = 15 ms, TR = 0.6 sec, and slice thickness = 5 mm.

$$S_{SE}(r, p_i) = k \cdot D(r) \cdot B_1(r) \cdot \sin^3\left(\frac{\pi}{2} \cdot \frac{p_i}{p_{\pi/2}} \cdot B_1(r)\right) \qquad [1]$$

where p_i is a function of the TX power, $p_{\pi/2}$ is the TX power corresponding to a 90° flip angle (usually calibrated at the center of the birdcage coil, i.e., at r = 0), D(r) is the proton spin density and k an arbitrary constant that depends on the gain of the MRI receiver circuit. In the presence of a uniform sample, the multipower MRI technique allows the mapping of the transmit and receive RF B_1 of the coil to be obtained with good accuracy over all the sample.

To experimentally evaluate the dependence of the RF B_1 field distribution on the sample dielectric properties (permittivity and conductivity) at 3 T, we used plastic cylinders (dia. 15 cm, length 38 cm) filled with: 1) a low dielectric constant vegetable oil, 2) distilled water, or 3) physiological saline solution. In the present work, for each sample 41 images were collected at incremented power levels with TE = 20 ms and TR = 4 sec (oil), TR = 20 sec (distilled water), and TR = 15 sec (saline). These pulse durations and repetition times were chosen to minimize

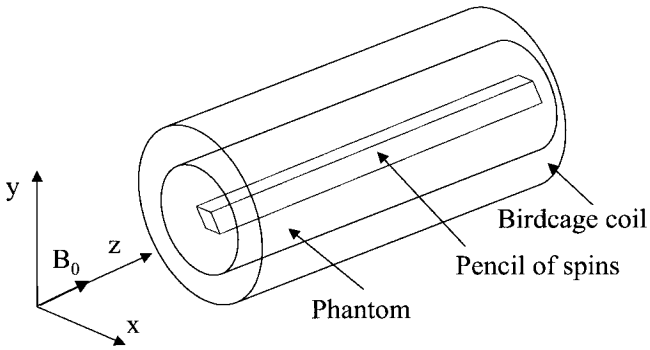

FIG. 2. The spatial orientation of the birdcage coil and the cylindrical phantoms.

T_1 and T_2 sample dependent effects. The high-power RF amplifier was verified for linearity of response over the TX range. The RF peak-to-peak pulse amplitude was measured by connecting the RF amplifier output to a high-frequency oscilloscope (Hewlet-Packard, HP54610B) via two cascaded high-power RF attenuators (Bird Electronic, Herts, UK) with total attenuation of 50 dB.

To simplify acquisition and analysis, the signal for B_1 mapping was acquired from a "pencil" of spins (1×1 cm, 51 cm long) aligned along the x-, y-, or z-axis of the birdcage. The axis orientations, with respect to the birdcage coil, used for B_1 mapping are reported in Fig. 2. In principle, the technique could be extended to a planar section of the sample at any orientation. The multipower MRI method was also used to map the transmit RF B_1 in the head of healthy volunteers (n = 3). Informed consent was obtained from all volunteers and the project was approved by the local ethics committee. In the B_1 mapping spin-echo pulse sequence (TE = 20 ms, TR = 8 sec, thickness 5 mm) no correction for CSF contamination was adopted but the TR was chosen long enough to minimize T_1-dependent effects in the gray and white matter.

A sinc RF pulse was used for B_1 mapping with the phantoms and with the head of volunteers. The pulse duration was 8 ms with oil, 4 ms with distilled water, 8 ms with saline, and 3.2 ms with the volunteers. These RF pulse duration times were necessary to avoid excessive reflected power and to achieve a sufficient range of flip angles in the different samples.

1D Analytical EM Simulation With Dielectric Slab

To qualitatively investigate the dependence of the RF B_1 distribution on the sample dielectric properties, we used a simple analytical EM model that considers a plane wave incident normally on a lossy slab of dielectric of thickness d (26). The RF field distribution $B_1(r)$ along the propagation axis is given by the superposition of the forward and reflected waves and was simulated according to (27):

$$B_1(r) \propto \sqrt{e^{-2\alpha r} + \Gamma_s^2 e^{+2\alpha r} + 2\Gamma_S \cos(2\beta \cdot r)} \qquad [2]$$

where r is the distance within the dielectric ($-d/2 \leq r \leq d/2$); α and β are the attenuation and the phase constants, respectively, which, for a given frequency, can be calculated from the permittivity and conductivity of the dielectric (26); and Γ_S is the modulus of the reflection coefficient of the slab. Γ_S takes a value from 0 to 1 and is a function of the operating frequency, the permittivity, the conductivity, and the thickness of the dielectric slab (26). The simulation was implemented using Matlab (MathWorks, Natick, MA) at an operating frequency of 128 MHz and with a slab of thickness of 16 cm composed of: vegetable oil ($\epsilon_r = 2.9$; $\sigma = 0$ S/m; $\Gamma_S = 0.12$); distilled water ($\epsilon_r = 74$; $\sigma = 0$ S/m; $\Gamma_S = 0.83$); or physiological saline solution ($\epsilon_r = 78$; $\sigma = 1.67$ S/m; $\Gamma_S = 0.81$) (28,29).

3D FD-TD EM Simulation With Phantoms and in a Head Model

The previous analytical EM model is useful for an intuitive understanding of RF B_1 penetration effects and RF B_1 standing wave effects at 3 T. However, a realistic simulation of the RF B_1 distribution in the human head requires an accurate dielectric model of the human head and powerful EM computational techniques. Several numerical EM techniques have been developed to evaluate the B_1 in the human head (7–13). In the present work, the finite difference time domain (FD-TD) method of calculation for electromagnetics was used. To solve Maxwell's equations for the electric and magnetic field components in a volume V, we enclose the volume V in a rectangular box and then divide the box into many small rectangular cells (Yee cells). This method has been described in detail previously (10,11).

The simulated data were obtained by considering an ideal bandpass 16-element birdcage coil and a shield with dimensions identical to those used in the experiment. For the empty coil, to allow a direct comparison with the pick-up probe data, the FD-TD simulation was implemented considering linear polarization of the RF coil along the x or y axis. Models of the cylindrical phantoms used in the MRI experiments were also created by assigning appropriate conductivity and permittivity for 128 MHz and considering quadrature polarization of the RF coil.

A 3D, anatomically accurate, multitissue model of the head (11) was also simulated inside the coil. The magnitude of the pertinent circularly polarized component of the RF (128 MHz) magnetic field was calculated along the coil axis. Yee cell dimensions were 2 mm in all dimensions for all calculations except for the calculation with the head where Δx (left-right direction) and Δy (anterior–posterior direction) were 2 mm and Δz (inferior–superior direction) was 2.5 mm. All calculations were set up and performed with the aid of commercially available software ("xfdtd"; Remcom, Inc.).

RESULTS AND DISCUSSION

The measured Q and S_{11} of the birdcage coil when empty, in the presence of the cylindrical phantoms, and with the coil loaded with the head of volunteers are reported in Table 1. The transmit peak power in the RF coil, corrected considering the matching of the birdcage, is reported in Table 1. The estimated RF amplitude at the center of the sample, $B_1(0)$, obtained from the multipower MRI-based technique, is also reported in Table 1. For comparison

Table 1
Birdcage Coil RF Parameters and RF B_1 Homogeneity at 3 T as a Function of the Sample Dielectric Properties and Orientation

Sample	S_{11} (dB)	Q[a]	Power (dB)[b]	$B_1(0)/B_1^{oil}$ (%)[c]	ΔX (cm)[d]	ΔZ (cm)[d]
Empty coil	−8	84	N.M.	N.M.	11	9
Oil	−5	60	49	100	15	10
Distilled water	−5	57	44	180	6	9
Saline	−35	23	58	33	11	8
Head	−24	27	52	67	10	7

[a]Measured as the ratio of the resonant frequency to the frequency bandwidth at −3 dB.
[b]Peak power coupled in the RF coil (78 dB corresponds to 4 kW), after correction considering the matching of the birdcage.
[c]Measured amplitude of the transverse circularly polarized RF magnetic field at the center of the birdcage coil, $B_1(0)$, normalized to that obtained with oil. At the coil center $B_1^{oil} = 0.73$ μT for a 90° flip angle and a pulse of 8 ms duration.
[d]Obtained from the measured B_1 distribution considering a maximum RF variation $\Delta B_1/B_1(0) = 10\%$.

purposes, the RF amplitude $B_1(0)$ was normalized considering an 8 ms pulse for all samples.

The accuracy of the multipower MRI method for B_1 mapping relies on the accurate setting of the RF power over the full TX range. We found that the RF power output was linear over a very wide TX range. Only a small saturation of the RF amplifier was observed (deviation from linearity less than 2%) for very high TX power. However, such small deviation from linearity does not introduce significant systematic errors in the measurement of the B_1 field.

1D Analytic Model

The results of the 1D analytical EM simulation of the B_1 distribution obtained at 128 MHz for a slab of dielectric composed of oil, distilled water, or saline solution are reported in Fig. 3. For comparison purposes in Fig. 3, the B_1 amplitude at the center of the slab was normalized to 100%. We found that the B_1 distribution is predicted to depend strongly on the electrical properties of the sample. This is due to a combination of RF penetration (conductivity-dependent) and standing wave (permittivity-dependent) effects. For the oil phantom (low dielectric constant) the simulated B_1 distribution is quite homogeneous (Fig. 3a) and resembles the expected distribution of the birdcage coil when empty. With oil the predicted region of B_1 uniformity (within 10% of the maximum) was about 32 cm (extrapolated from the data of Fig. 3a). However, with distilled water (high dielectric constant and zero conductivity) the wavelength of the EM radiation is reduced ($\lambda = \lambda_0/\sqrt{\mu\epsilon} = 27$ cm) with respect to the free space wavelength at 128 MHz ($\lambda_0 = 234$ cm). Since $\lambda/2$ becomes comparable with the thickness of the sample (16 cm), there is a considerable phase-shift of the B_1 field within the slab. This produces a very inhomogeneous RF distribution (Fig. 3b), with a typical standing wave pattern and a pronounced maximum at the center. The predicted region of B_1 uniformity (within 10% of the maximum) was about 3.9 cm. With the saline solution (high dielectric constant and high conductivity) the RF B_1 distribution shown in Fig. 3c presents two minima located symmetrically with respect to the center of the slab. In Fig. 3c the minimum on the left side of the slab is not well resolved because of a linear trend in the data. This asymmetry originates from the assumption in the 1D analytical model that the plane wave is incident from the left to the right of the slab. The estimated region of B_1 uniformity (within 10% of the maximum) was about 6.8 cm. With the saline solution the combination of RF standing wave effects and RF attenuation effects (due to induced RF eddy currents in the sample) plays an important role and the RF homogeneity is somewhat improved in the central region. However, it is worth noting that the position and depth of the two minima in the RF distribution are influenced by the operating frequency, sample thickness, permittivity, and conductivity of the sample.

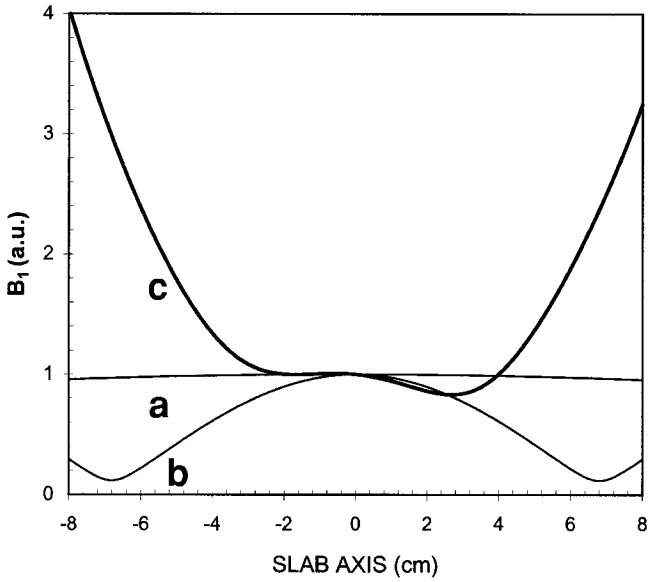

FIG. 3. The 1D analytical simulation of the RF B_1 distribution obtained at 128 MHz for a slab of dielectric of thickness 16 cm composed of: vegetable oil (**a**) ($\epsilon_r = 2.9$); distilled water (**b**) ($\epsilon_r = 74$; $\sigma = 0$ S/m); and physiological saline solution (**c**) ($\epsilon_r = 78$; $\sigma = 1.67$ S/m). For comparison purposes the B_1 amplitude at the center of the slab was normalized to 100%.

3D Results x-y Plane

The measured and FD-TD simulation of the RF B_1 distribution at 128 MHz in the transverse plane ($B_1(x)$ or $B_1(y)$) obtained with the empty coil and with the cylinder containing oil are reported in Fig. 4. For comparison purposes the B_1 amplitude at the center of the coil was normalized to 100%. As shown in Fig. 4, there is good agreement

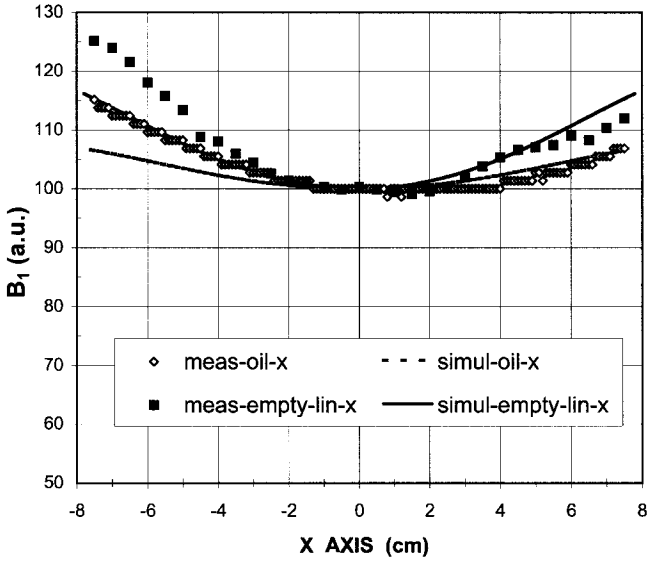

FIG. 4. The measured and FD-TD simulated RF B_1 distribution in the transverse direction obtained at 128 MHz for the empty birdcage coil and in the presence of a cylinder (dia. 15 cm, length 38 cm) filled with oil. For comparison purposes the B_1 amplitude at the center of the coil was normalized to 100%.

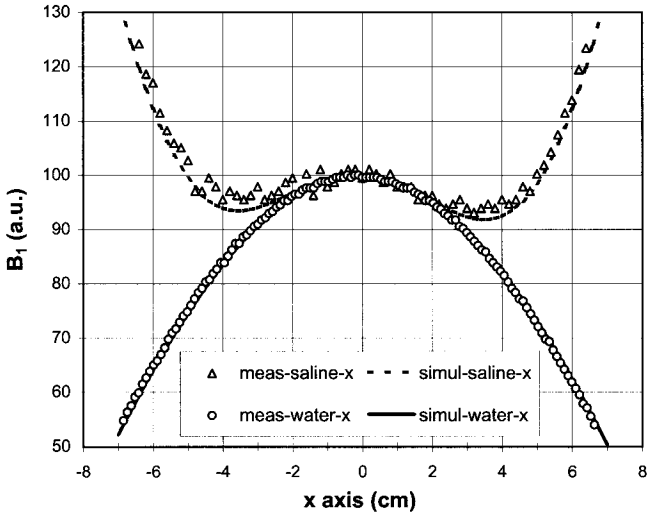

FIG. 5. The measured and FD-TD simulated RF B_1 distribution in the transverse direction obtained at 128 MHz for the birdcage in the presence of a cylinder (dia. 15 cm, length 38 cm) filled with distilled water or saline solution. For comparison purposes the B_1 amplitude at the center of the coil was normalized to 100%.

between the measured and simulated data (maximum deviation less than 10%). With oil, in contrast to the simple 1D analytical EM model, the numerical FD-TD simulation predicts a minimum of the RF distribution at the center of the sample. This minimum is probably due to the "intrinsic" B_1 distribution of the birdcage coil when empty, as confirmed by the experimental data obtained with the pick-up probe (Fig. 4). It is worth noting that there is a small asymmetry (left–right) in the measured data. As reported in Table 1, the measured region of RF uniformity (within 10% of the value at the center) was about 11 cm diameter with the empty coil (linear mode) and 15 cm diameter with oil (quadrature mode).

Figure 5 shows the measured and numerical simulation of the RF B_1 distribution in the transverse direction with the cylinder containing distilled water or saline solution. For comparison purposes the B_1 amplitude at the center of the coil was normalized to 100%. We found that at 3 T in the transverse plane the B_1 distribution depends strongly on the electrical properties of the sample and that it is qualitatively similar to the simple analytical simulation reported in Fig. 3. According to the analytical model, the B_1 distribution is due to a combination of RF penetration and standing wave effects. As shown in Fig. 5, with distilled water the B_1 distribution presents a maximum at the center of the coil, which is due to the standing wave effect only. With the saline solution the RF attenuation effect does counterbalance, partially, the RF inhomogeneity due to the standing wave effect. For this reason, with saline the RF distribution exhibits two minima located symmetrically with respect to the center and the RF homogeneity improves in the central region of the sample. The measured region of RF uniformity (within 10% of the maximum) was about 6 cm diameter with distilled water and about 11 cm diameter with saline. As shown in Fig. 5, there is good agreement between the simulated and one or the other side of the measured plots (deviation <5%) for the two samples.

3D Results z-Axis

The measured and simulated B_1 distributions along the z-axis of the birdcage coil when empty and with the cylinder containing oil, distilled water, or saline are reported in Fig. 6. For comparison purposes the B_1 amplitudes at the center of the coil were normalized to 100%. As shown in Fig. 6, there is good agreement between the measured

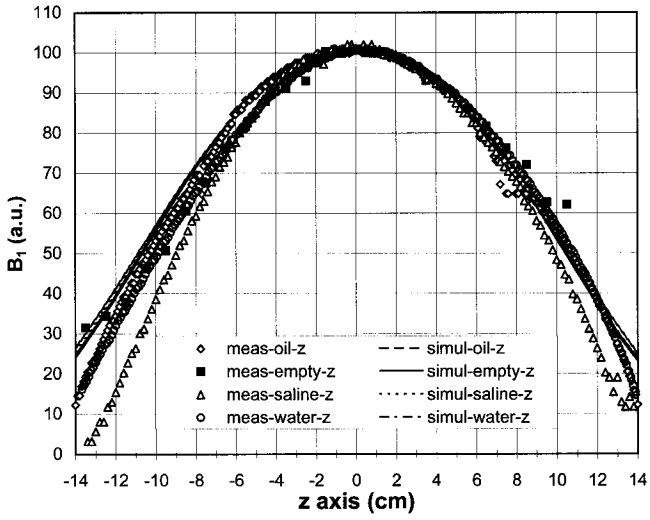

FIG. 6. The measured and FD-TD simulated RF B_1 distribution along the z-axis obtained at 128 MHz for the empty RF coil and in the presence of cylinders (dia. 15 cm, length 38 cm) filled with oil, distilled water, or saline solution. For comparison purposes the B_1 amplitude at the center of the coil was normalized to 100%.

and FT-DT simulated data (deviation <10%) for all samples, with the exception of saline solution, which exhibits a slightly narrower B_1 distribution and a deviation from the theoretical plot, which is less than 20%. We found a very similar z-axis B_1 distribution in the coil when empty and when loaded with the cylindrical phantoms. The B_1 amplitude presents a maximum in the mid-plane of the coil and a substantial decrease at the two ends of the coil. The measured regions of axial RF uniformity (within 10% of the maximum) was about 9 cm (see Table 1).

It has been shown previously that a cylindrical phantom containing water solutions can present a true "dielectric resonance" which can be used as an RF resonator for high-field MRI experiments (30). The "dielectric resonance" can be sustained by any of several resonant modes ($TE_{01\delta}$, $TM_{01\delta}$, $HEM_{11\delta}$) whose frequency is a function of the dielectric constant, the diameter, and the length of the cylinder. Equations have been derived for calculating the resonance frequency of dielectric resonators (30). Considering the cylindrical phantom used in the present work (dia. 15 cm, length 38 cm) filled with distilled water (ϵ_r = 74) the lowest dielectric resonance frequency is about 192 MHz. This excludes the presence of true dielectric resonance effects in the RF B_1 distribution reported here (Figs. 4–7). Moreover, supposing the presence of a dielectric mode ($TM_{01\delta}$ or $HEM_{11\delta}$) at 127.3 MHz, the B_1 distribution along the z-axis for the empty coil (or with oil) should be significantly different from that obtained in the presence of the water cylinder. However, the experimental results reported in Fig. 6 show that the axial B_1 distribution of the empty coil (or with oil) was practically identical to that obtained with the water phantom. These findings confirm that true dielectric resonance effects with samples of the size of the human head are not present at 3 T. Experimental evidence of true dielectric resonance (labeled B_1-eigenfield) at 170 MHz has been recently reported with phantoms and in the human head (31).

In Vivo Results

The measured and simulated B_1 distributions in the transverse direction and in the axial direction in the head of a volunteer are reported in Fig. 7. For comparison purposes the B_1 amplitudes at the center of the coil were normalized to 100%. As shown in Fig. 7a,b, there is very good agreement between experimental and simulated data in the transverse direction (deviation <5%). The transverse RF distribution in the head exhibits two minima located symmetrically with respect to the maximum central value. The measured transverse RF uniformity in the head (within 10% of the center) was about 10 cm in diameter. Note that the shape of the transverse RF distribution in the head is very similar to that obtained with saline solution. However, a better RF homogeneity was measured in the head, this probably being due to the heterogeneous structure of the tissues which reduce the effect of RF eddy currents. These findings are in agreement with earlier numerical 3D simulations (8). The axial RF distributions reported in Fig. 7c,d show that there is good agreement between experimental and simulated data in the central region (deviation <10%). However, at the inferior end of the coil the difference between measured and simulated data reaches a maximum of about 20%. The measured RF distribution in the head is very similar to that obtained with saline. The measured axial RF uniformity (within 10% of the center) in the head was about 7 cm.

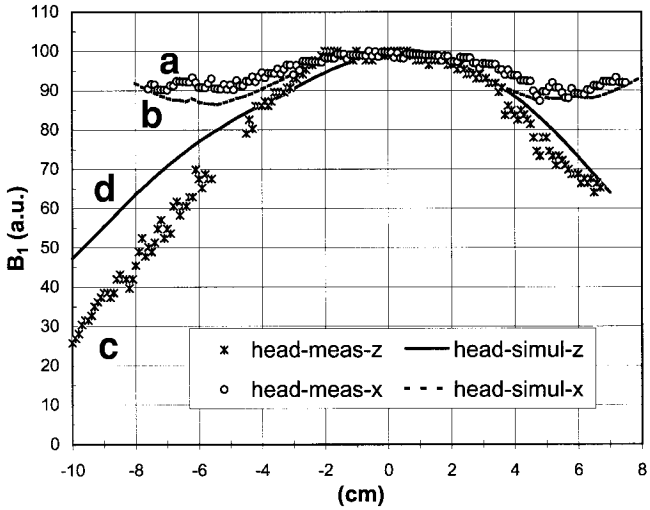

FIG. 7. The measured (**a**) and FD-TD simulated (**b**) RF B_1 distribution obtained at 128 MHz in the head of a volunteer along the transverse (left-right) direction. The measured (**c**) and FD-TD simulated (**d**) RF B_1 distribution in the head of a volunteer along the z-axis (inferior–superior). For comparison purposes the B_1 amplitude at the center of the coil was normalized to 100%.

As shown in Table 1, the normalized amplitude of the RF magnetic field at the center of the birdcage coil, $B_1(0)$, depends on the dielectric properties of the sample. It is worth noting that with distilled water the measured $B_1(0)$ is about 1.8 times the value obtained with the oil sample. This increase of $B_1(0)$ with distilled water is probably due to pure standing wave effects. However, with saline solution (or the human head) the measured $B_1(0)$ decreases because of RF eddy currents losses induced in the sample.

CONCLUSIONS

We have reported the RF B_1 distribution in cylindrical phantoms and in the head of healthy volunteers using a 3 T MRI research system equipped with a birdcage coil. We found that, with the phantoms and in vivo, the RF B_1 distribution in the transverse plane is strongly dependent on the dielectric properties of the sample. We have shown that this can be explained as a combination of RF penetration and RF standing wave effects. However, at 3 T the measured B_1 distribution in the x–y plane shows that in the whole head the B_1 variation is less than 15%. In contrast, along the coil z-axis (coronal/sagittal plane) the RF B_1 distribution is determined mainly by the RF coil geometry. Experimental results along that axis show only a very small dependence on the dielectric properties (conductivity) of the sample. We found that in the head the axial RF homogeneity (within 10%) is about 7 cm, this corresponds to only 33% of the coil's length. This suggests that at 3 T a careful positioning of the head within the coil is very important for signal optimization. Moreover, tech-

niques for improving the intrinsic axial RF homogeneity of birdcage coils should be employed at 3 T (32).

The accurate B_1 map obtained with the phantoms and in vivo can be used for a priori MRI correction techniques. For example, it has been shown recently that by actively modulating the TX power as function of the axial slice position it is possible to partly compensate for axial B_1 inhomogeneity of 3 T birdcage coils (33). Moreover, the knowledge of the B_1 spatial distribution at 3 T is of importance for a posteriori MRI correction techniques such as relaxation time measurements (34) and image segmentation (35). As an additional application, accurate RF B_1 mapping may also find use in low frequency (100–300 MHz) EPR imaging and Overhauser MRI (36).

In conclusion, we have quantitatively characterized RF B_1 distortion in several phantoms and in the human head at 3 T in a head-sized birdcage coil. The good agreement between calculation and experiment demonstrates that B_1 distortion at high field can be explained with 3D full-Maxwell calculations. The minor disagreement between the calculation and the experiment could be due to limited accuracy in assumed electrical properties for all the materials, limitations in the calculation method, and modeling techniques, and in the intrinsic error in any experimental measurements. Both the experimental and theoretical results reported here show that the B_1 distribution in the transverse plane is strongly dependent on the dielectric properties of the sample. In contrast, along the birdcage coil z-axis the B_1 distribution is determined mainly by the coil geometry.

ACKNOWLEDGMENTS

We thank Prof. Paul Matthews for his continued support and encouragement. We thank Mr. David A. Homfray for assistance with this project. We also thank the EU BIOMED programme for grant funding (to M.A.), and the UK MRC (to P.J.).

REFERENCES

1. Edelstein WA, Glower GH, Hardy CJ, Redington RW. The intrinsic signal-to-noise-ratio in NMR imaging. Magn Reson Med 1986;3:604–618.
2. Jezzard P, Balaban RB. Correction for geometric distortion in echo planar images from B_0 field variations. Magn Reson Med 1995;34:65–73.
3. Glover GH, Hayes CE, Pelc NJ, Edelstein WA, Muller OM, Hart HR, Hardy CJ, O'Donnell M, Barber WD. Comparison of linear and circular polarization for magnetic resonance imaging. J Magn Reson 1985;64:255–270.
4. Bomsdorf H, Henzel T, Kunt D, Roeschmann P, Tschendel O, Wieland J. Spectroscopy and imaging with a 4 Tesla whole-body MR system. NMR Biomed 1988;1:151–158.
5. NRPB. Board statement: Advice on the 1998 ICNIRP guidelines for limiting exposure to time-varying electric, magnetic and electromagnetic fields (up to 300 GHz). NRPB 1998;10(2).
6. FDA. Guidance for the submission of premarket notifications for magnetic resonance diagnostic devices. FDA; Nov. 14, 1998.
7. Simunic D, Wach P, Renhart W, Stollberger R. Spatial distribution of high-frequency electromagnetic energy in human head during MRI: numerical results and measurements. IEEE Trans Biomed Eng 1996;43:88–94.
8. Jin JM, Chen J, Chew WC, Gan H, Magin RL, Dimbylow PJ. Computation of electromagnetic fields for high-frequency magnetic resonance imaging applications. Phys Med Biol 1996;41:2719–2738.
9. Chen J, Feng Z, Jin JM. Numerical simulation of SAR and B_1-field inhomogeneity of shielded RF coils loaded with the human head. IEEE Trans Biomed Eng 1998;45:650–659.
10. Collins CM, Li S, Smith MB. SAR and B_1 field distributions in a heterogeneous human head model within a birdcage coil. Magn Reson Med 1998;40:847–856.
11. Collins CM, Smith MB. Calculated B_1 homogeneity, SNR, and SAR vs frequency for the head in a idealized quadrature birdcage coil. In: Proc ISMRM 1999;7:417.
12. Jin JM. Electromagnetic analysis and design in magnetic resonance imaging. Boca Raton, FL: CRC Press; 1999.
13. Gandhi OP, Chen XB. Specific absorption rates and induced current densities for an anatomy based model of the human for exposure to time-varying magnetic fields of MRI. Magn Reson Med 1999;41:816–823.
14. Hayes CE, Edelstein WA, Schenck JF, Mueller OR, Eash M. An efficient, highly homogeneous radiofrequency coil for whole body NMR imaging at 1.5 T. J Magn Reson 1985;63:622–628.
15. Foo TKF, Hayes CE, Kang YW. An analytical model for the design of RF resonators for MR body imaging. Magn Reson Med 1991;21:165–177.
16. Chen C, Hoult DJ. Biomedical magnetic resonance technology. Bristol: IOP; 1989.
17. Fakri-Bouchet L, Lapray C, Briguet A. Measurements of the radiofrequency field in magnetic resonance coils. Meas Sci Technol 1998;9:1641–1646.
18. Murphy-Boesch J, So GJ, James TL. Precision mapping of the B_1 field using the rotating-frame experiment. J Magn Reson 1987;73:293–303.
19. Hornak JP, Szumonwski J, Bryant RG. Magnetic field mapping. Magn Reson Med 1988;6:158–163.
20. Insko EK, Bolinger L. Mapping of the radiofrequency field. J Magn Reson Series A 1993;103:82–85.
21. Jerschow A, Bodenhausen G. Mapping the B_1 field distribution with non ideal gradients in a high-resolution NMR spectrometer. J Magn Reson 1999;137:108–115.
22. Topp S, Adalsteinssonn E, Spielman DM. Fast multislice B_1-mapping. In: Proc ISMRM; 1997:281.
23. Sled JS, Bruce G. Standing-wave and RF penetration artefacts caused by elliptic geometry: an electrodynamic analysis of MRI. IEEE Trans Med Imag 1998;17:653–662.
24. Barker GJ, Simmons S, Arridge SR, Tofts PS. A simple method for investigating the effects of non-uniformitty of radiofrequency transmission and radiofrequency reception in MRI. Br J Radiol 1998;71:59–67.
25. Barberi EA, Gati JS, Rutt BK, Menon RS. A transmit-only/receive-only (TORO) RF system for high-field MRI/MRS applications. Magn Reson Med 2000;43:284–289.
26. Stratton JA. Electromagnetic theory. New York: McGraw-Hill; 1941.
27. Balanis A. Advanced engineering electromagnetics. New York: Wiley Press; 1989.
28. Tofts PS, Barker GJ, Dean TL, Gallagher H, Gregory AP, Clarke RN. A low dielectric constant customised phantom design to measure RF coil nonuniformity. Magn Reson Imag 1997;15:69–75.
29. Schwan HP. Electrical properties of tissues and cell suspensions. Adv Biol Med Phys 1957;5:147–209.
30. Wen H, Jaffer FA, Denison TJ, Duewell S, Chesnick AS, Balaban RS. The evaluation of dielectric resonators containing H_20 or D_2O as RF coils for high-field MR imaging and spectroscopy. J Magn Reson Series B 1996;110:117–123.
31. Roeschmann P. Role of B_1-eigenfields of dielectric objects in high-field MRI. In: Proc ISMRM, 2000;8:151.
32. Alecci M, Jezzard P. Use of endcap for improving the axial RF field homogeneity of a 3 tesla birdcage coil. In: London: British Chapter ISMRM Abstracts; 1999.
33. Clare S, Alecci M, Jezzard P. B_1 inhomogeneity compensation by active transmit power modulation. In: Proc ISMRM 1999;7:1976.
34. Clare S, Jezzard P. Fast T_1 mapping using multislice EPI. In: Proc ISMRM, Denver, 2000;8:430.
35. Alecci M, Zhang Y, Brady JM, Jezzard P, Smith S, Image-based evaluation of *a-priori* B_1 field correction and its effect on MRI tissue segmentation. In: Proc ISMRM 2000;8:109.
36. Alecci M, Seimenis I, McCallum SJ, Lurie DJ, Foster MA. Nitroxide free radical clearance in the live rat monitored by radio-frequency CW EPR and PEDRI. Phys Med Biol 1998;43:1889–1906.